Medical Physics
The International Journal of Medical Physics Research and Practice

Optimization of a dual-energy contrast-enhanced technique for a photon-counting digital breast tomosynthesis system: I. A theoretical model

Ann-Katherine Carton, Christer Ullberg, Karin Lindman, Raymond Acciavatti, Tom Francke, and Andrew D. A. Maidment

Citation: Medical Physics **37**, 5896 (2010); doi: 10.1118/1.3490556
View online: http://dx.doi.org/10.1118/1.3490556
View Table of Contents: http://scitation.aip.org/content/aapm/journal/medphys/37/11?ver=pdfcov
Published by the American Association of Physicists in Medicine

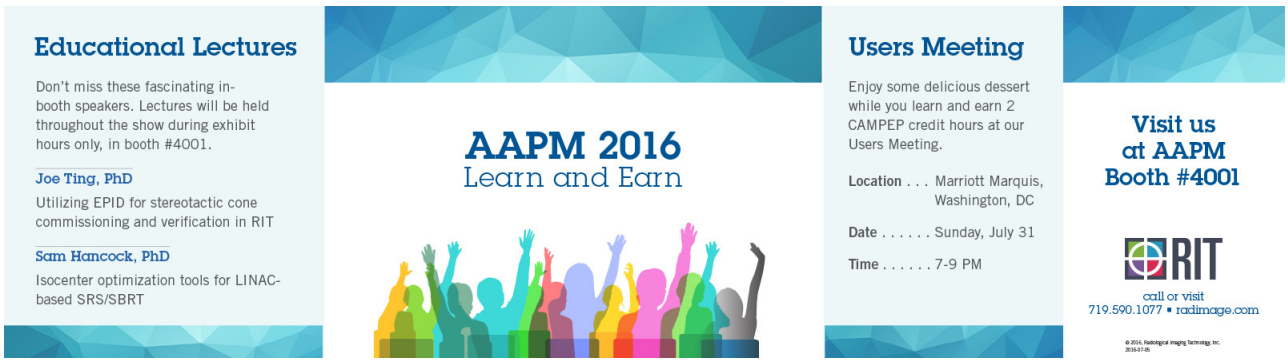

Optimization of a dual-energy contrast-enhanced technique for a photon-counting digital breast tomosynthesis system: I. A theoretical model

Ann-Katherine Carton
University of Pennsylvania, Philadelphia, Pennsylvania 19104

Christer Ullberg and Karin Lindman
XCounter AB, Svärdvägen 11, SE-182 33 Danderyd, Sweden

Raymond Acciavatti
University of Pennsylvania, Philadelphia, Pennsylvania 19104

Tom Francke
XCounter AB, Svärdvägen 11, SE-182 33 Danderyd, Sweden

Andrew D. A. Maidment[a)]
University of Pennsylvania, Philadelphia, Pennsylvania 19104

(Received 22 August 2009; revised 29 August 2010; accepted for publication 30 August 2010; published 20 October 2010)

Purpose: Dual-energy (DE) iodine contrast-enhanced x-ray imaging of the breast has been shown to identify cancers that would otherwise be mammographically occult. In this article, theoretical modeling was performed to obtain optimally enhanced iodine images for a photon-counting digital breast tomosynthesis (DBT) system using a DE acquisition technique.

Methods: In the system examined, the breast is scanned with a multislit prepatient collimator aligned with a multidetector camera. Each detector collects a projection image at a unique angle during the scan. Low-energy (LE) and high-energy (HE) projection images are acquired simultaneously in a single scan by covering alternate collimator slits with Sn and Cu filters, respectively. Sn filters ranging from 0.08 to 0.22 mm thickness and Cu filters from 0.11 to 0.27 mm thickness were investigated. A tube voltage of 49 kV was selected. Tomographic images, hereafter referred to as DBT images, were reconstructed using a shift-and-add algorithm. Iodine-enhanced DBT images were acquired by performing a weighted logarithmic subtraction of the HE and LE DBT images. The DE technique was evaluated for 20–80 mm thick breasts. Weighting factors, w_t, that optimally cancel breast tissue were computed. Signal-difference-to-noise ratios (SDNRs) between iodine-enhanced and nonenhanced breast tissue normalized to the square root of the mean glandular dose (MGD) were computed as a function of the fraction of the MGD allocated to the HE images. Peak SDNR/$\sqrt{\text{MGD}}$ and optimal dose allocations were identified. SDNR/$\sqrt{\text{MGD}}$ and dose allocations were computed for several practical feasible system configurations (i.e., determined by the number of collimator slits covered by Sn and Cu). A practical system configuration and Sn–Cu filter pair that accounts for the trade-off between SDNR, tube-output, and MGD were selected.

Results: w_t depends on the Sn–Cu filter combination used, as well as on the breast thickness; to optimally cancel 0% with 50% glandular breast tissue, w_t values were found to range from 0.46 to 0.72 for all breast thicknesses and Sn–Cu filter pairs studied. The optimal w_t values needed to cancel all possible breast tissue glandularites vary by less than 1% for 20 mm thick breasts and 18% for 80 mm breasts. The system configuration where one collimator slit covered by Sn is alternated with two collimator slits covered by Cu delivers SDNR/$\sqrt{\text{MGD}}$ nearest to the peak value. A reasonable compromise is a 0.16 mm Sn–0.23 mm Cu filter pair, resulting in SDNR values between 1.64 and 0.61 and MGD between 0.70 and 0.53 mGy for 20–80 mm thick breasts at the maximum tube current.

Conclusions: A DE acquisition technique for a photon-counting DBT imaging system has been developed and optimized. © *2010 American Association of Physicists in Medicine*.
[DOI: 10.1118/1.3490556]

Key words: digital breast tomosynthesis, iodine contrast-enhanced imaging, dual-energy, spectral optimization, signal-difference-to-noise

I. INTRODUCTION

Tumor growth and metastasis are accompanied by the development of new blood vessels having increased permeability.[1] As a result, the absorption of vascular contrast agents is often different in cancerous breast tissue than in normal and benign breast tissues. Today, the gold standard for imaging breast cancer vascularity and perfusion is contrast-enhanced magnetic resonance imaging (CE-MRI). CE-MRI is a three-

dimensional (3D) technique that uses a gadolinium chelate as the vascular contrast agent. Clinical diagnosis with CE-MRI relies on the analysis of morphological features and vascular enhancement kinetics;[2–4] however, no consensus exists in the literature as to which feature is most informative. Current MRI pulse sequences trade-off spatial and temporal resolution, allowing interpretation strategies that emphasize either morphological features or vascular enhancement kinetics. The American Cancer Society recommends CE-MRI as an adjunct to mammography for screening women at high risk of developing breast cancer;[5] however, widespread use of CE-MRI as a screening tool is unlikely due to various technical challenges, limited availability, and prohibitive cost.[6]

X-ray imaging with an iodinated contrast agent can also demonstrate changes in breast vascularity. Contrast-enhanced x-ray imaging of the breast has been extensively investigated since the early 1980s.[7–9] Contrast-enhanced computed tomography, using a conventional body scanner,[7] contrast-enhanced mammography,[8] and contrast-enhanced digital subtraction angiography of the breast using an x-ray image intensifier-based angiography system,[9] has been proposed. However, each of these technologies was impractical for clinical use due to one or more of the following reasons: High radiation dose, limited spatial resolution, and impracticalities of image handling.

The advent of high temporal resolution and high spatial resolution full-field digital mammography (DM), digital breast tomosynthesis (DBT), and dedicated breast computed tomography (BCT) has opened the possibility for improved CE breast x-ray imaging techniques.[10] CE-DM,[11–20] CE-DBT,[21–28] and CE-BCT[29,30] are under investigation. These modalities integrate morphological and kinetic features in diagnostic images at low radiation dose with higher temporal and spatial resolution than CE-MRI. CE-DBT and CE-BCT provide the further benefit of tomographic imaging, similar to CE-MRI, whereas CE-DM provides projection images that do not depict the 3D morphology and location of contrast-enhanced lesions. Most importantly, CE x-ray imaging is based on a technology that is fundamentally less expensive than CE-MRI and thus has the potential to be more widely available.

Two CE x-ray imaging techniques have been proposed: Temporal[11,12,15,17,21–23] and dual-energy (DE) subtraction.[13,16–20,24,25] Both techniques take advantage of the variation of iodine attenuation as a function of energy; the attenuation of iodine is 5.5 times larger above the K-edge of iodine than below the K-edge of iodine. In temporal subtraction, the breast is imaged before and after administration of an iodinated contrast agent using a high-energy (HE) x-ray spectrum with energies predominantly above the K-edge of iodine (33.2 keV). Iodine enhancement images are produced by subtracting the logarithm of the precontrast and postcontrast images, yielding images in which the signal intensity (SI) is proportional to the iodine concentration. In DE subtraction, low-energy (LE) and HE image pairs are acquired after contrast injection at energies that closely bracket the K-edge of iodine. Iodine enhancement images are produced as the weighted difference of the logarithms of the LE and HE images.

In the absence of breast motion, temporal subtraction is the most sensitive method to measure the uptake of iodinated contrast agents, since the background breast tissue can be completely cancelled and only areas with contrast agent remain visible in the subtracted images. However, in practice, temporal subtraction CE x-ray images demonstrate significant breast-motion artifacts in the subtraction images due to the extended time (up to 10 min) between the acquisition of the precontrast and postcontrast series.[12,27,28] Motion artifacts affect the measurement accuracy of the x-ray transmission of the iodine contrast agent, resulting in erroneous iodine quantification[21] and a reduction in lesion morphology detail. Conversely, with DE techniques, there is less subject contrast and residual breast tissue may be visible lessening the conspicuity of contrast agent uptake; however, patient motion artifacts can be reduced substantially[27,28] because iodine enhancement images are obtained from HE and LE x-ray images of the breast that are acquired simultaneously or in rapid succession. At this time, resilience to motion artifacts makes DE imaging more favorable than temporal subtraction despite the lower inherent sensitivity. In the future, appropriate motion correction algorithms may be developed for temporal subtraction CE images.[31]

This paper investigates a DE technique to produce iodine-enhanced images using a photon-counting DBT system. A system design is proposed that allows the simultaneous acquisition of LE and HE images in a single scan. Sn and Cu filtration are used to produce LE and HE images, respectively. A theoretical model of the imaging system is used to optimize the weighting factors for the logarithmic subtraction and the key acquisition parameters including the Sn and Cu filter thickness, the dose allocation between the LE and HE images, and the mean glandular dose, while accounting for the limitations of the x-ray tube. The analysis is performed for 20–80 mm thick breasts of various compositions.

II. MATERIALS AND METHODS

II.A. System description

II.A.1. Acquisition system

The current research was conducted using an XC Mammo-3T photon-counting DBT system (XCounter AB, Danderyd, Sweden) described in detail previously.[32–36] The system is shown in Fig. 1. The system consists of a W-target x-ray source (RAD 70T, Varian Medical Systems, Salt Lake City, UT) mounted opposed to a camera consisting of 48 photon-counting, orientation sensitive, linear gas detectors. Each detector is precisely aligned with the focal spot of the x-ray source. A prepatient collimator is positioned above the breast and defines 48 fan-shaped beams, each aligned with a detector and the x-ray focal spot. The x-ray tube, prepatient collimator, and camera are mounted on an E-arm that is translated across the breast in a continuous linear motion. Each linear detector collects a projection image of the breast

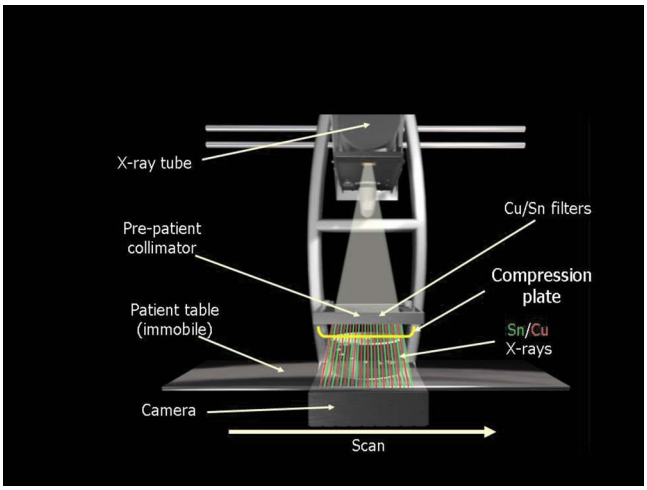

FIG. 1. Design principle of the photon-counting XC Mammo-3T (XCounter AB, Danderyd, Sweden). The x-ray tube, prepatient collimator, and camera (consisting of 48 linear detectors) are mounted on an E-arm. The prepatient collimator is used to define 48 fan-shaped beams; each is precisely aligned with the x-ray tube and a detector. Images are produced by linearly scanning the E-arm past the breast; in the process, 48 images of the breast are produced, each at a unique angle. The dual-energy implementation was obtained by differentially filtering the 48 fan beams by Sn and Cu. In this way, LE and HE images are obtained simultaneously in a single scan. In the shown configuration, one Sn filter is alternated by one Cu filter. As such, 24 detectors capture a LE image and 24 detectors capture a HE image. Other system configurations are obtained by alternately filtering a different number of fan beams with Sn or Cu.

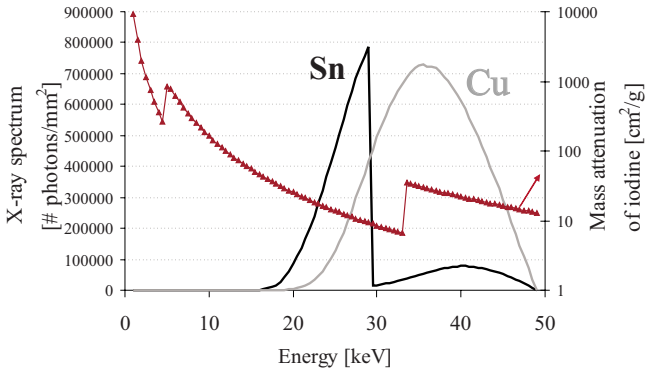

FIG. 2. Illustration of a Sn (LE) and Cu (HE) en x-ray spectrum detected by the XC-Mammo 3T XCounter detector after transmission through a 20 mm thick breast.

at a distinct angle. Thus in a single scan, 48 projection images are acquired simultaneously; each projection differs by approximately 0.5°. The linear detectors occupy an active area of 24×30 cm^2. The pixel size is 60×60 μm^2. The detectors are translated at 3 cm/s and read out every 2 ms during the scan.

The detector design provides several advantages that have been described in previous papers.[32–36] Briefly summarized, (i) the precise alignment of each detector with the prepatient collimator and focal spot results in almost perfect scatter rejection in the object; (ii) the detector is quantum-noise limited and does not contribute any electronic noise; the strong gaseous amplification of each photon interaction allows a simple threshold to exclude electronic noise from being counted and included in the final image; (iii) the amount of detector-to-detector scatter and detector-to-detector fluorescence is low; (iv) the modulation transfer function is determined solely by the detector element size, scanning unsharpness, and geometric factors; (v) each line of the image is rapidly acquired (typically <2 ms), minimizing any motion blurring; (vi) the large number of simultaneously acquired images significantly reduces tomographic reconstruction artifacts; and (vi) the detector technology is free of lag and has very high dynamic range.

II.A.2. Dual-energy implementation

The design of the XC Mammo-3T allows for the simultaneous acquisition of LE and HE projection images in a single scan by differentially filtering the 48 fan beams (Fig. 1). Sn filtration was used to produce LE images and Cu filtration was used to produce HE images. The selection of Sn and Cu was based on practical considerations such as the availability and durability of high purity foil filters with homogenous thickness.[24] The number of fan beams that are alternately filtered with Sn and Cu determines the signal-difference-to-noise ratio (SDNR) of the resulting subtraction images. With this in mind, several system configurations were investigated.

Simultaneous image acquisition minimizes the risk of patient motion but requires that the LE and HE images be acquired with the same target material and kV. The investigation was performed at 49 kV, the highest kV possible with the RAD 70T mammography x-ray tube. Preliminary theoretical calculations have shown that this kV was necessary to obtain sufficiently high photon fluence. Figure 2 illustrates LE and HE spectra obtained by filtering a 49 kV W-target x-ray beam with a 0.16 mm Sn filter or a 0.23 mm Cu filter. The spectra were calculated using a validated extrapolation of Boone's model.[21,37] At 49 kV, the acquisition time for a single scan is 10 s.

The 48 projection images were flat fielded to correct for spatial variations in gain and in the intensity of the x-ray beam, 2×2 pixel binning was applied to obtain 120×120 μm^2 pixels. Binning increases per-pixel signal-to-noise by a factor of 2, although it reduces spatial resolution.

II.A.3. Tomographic image reconstruction

Tomographic reconstruction is performed using a shift-and-add algorithm.[38] Cross-sectional images (hereafter referred to as *DBT images)* are reconstructed parallel to the detector array with 1 mm spacing. DBT images are calculated as

$$\mathrm{SI} = N \times \exp\left(\frac{1}{N}\sum_{n=1}^{N} P_n\right), \tag{1}$$

where SI is the per-pixel signal intensity in the DBT images, P_n is the per-pixel signal intensity in the appropriately shifted and resampled nth projection image (Appendix A),

and N is the total number of projections used to generate the DBT images.

The in-plane pixel size was 120×120 μm^2. The pixel depth of the DBT images is 16 bits.

II.A.4. Image processing

Iodine-enhanced DBT images (hereafter referred to as *DE-DBT images)* are produced by weighted logarithmic subtraction of the Cu and Sn DBT images

$$\mathrm{SI_{DE}} = \ln[\mathrm{SI_{Cu}}] - w_t \cdot \ln[\mathrm{SI_{Sn}}], \tag{2}$$

where $\mathrm{SI_{DE}}$, $\mathrm{SI_{Cu}}$, and $\mathrm{SI_{Sn}}$ denote the per-pixel signal intensity in the DE, Cu, and Sn DBT images, respectively. The weighting factor w_t is optimized to cancel the breast tissue background in the DE-DBT image.

The weighted logarithmic subtraction was performed on the DBT images because each LE and HE projection image is acquired at a unique angle, making it impossible to subtract the Sn and Cu projection images. However, the DBT images differ with the number of projection images and acquisition geometry. Based on a previous work where the difference in the image content between DBT images reconstructed with 24 and 48 projection images was compared, these image differences are expected to be insignificant.[36] An in depth study of possible misregistration artifacts is, however, outside of the scope of this paper.

II.B. System simulation

A computer model was created to simulate the DE implementation of the XC Mammo-3T system. The model is based on the differential attenuation of x rays. The signal recorded per pixel in the nth Sn and Cu projection images, $P_{\mathrm{Sn},n}$ and $P_{\mathrm{Cu},n}$, is the natural logarithm of the number of primary x rays absorbed in the detector

$$P_{m,n}(f_g, I) = \ln\left[\sum_{i=1\ \mathrm{keV}}^{49\ \mathrm{keV}} S_m(E_i) e^{-\alpha_i \sec\theta_n}(1 - e^{-\beta_i})\Delta E\right], \tag{3}$$

where m denotes Sn or Cu, f_g refers to the fraction of glandular tissue, I indicates the iodine concentration, $S_m(E_i)$ is the photon fluence at energy E_i of the Sn or Cu spectrum at the breast entrance, and θ_n denotes the angle between the incident x-ray beam and the normal to the detector for the nth projection image. The additional terms α_i and β_i have been defined as

$$\alpha_i \equiv \mu_{\mathrm{Skin}}(E_i) t_{\mathrm{Skin}} + \mu_g(E_i) t_g + \mu_f(E_i) t_f + \mu_I(E_I) t_I, \tag{4}$$

$$\beta_i \equiv \mu_{\mathrm{Gas}}(E_i) t_{\mathrm{Gas}}. \tag{5}$$

Concerning the subscripts of the linear attenuation coefficient μ and thickness t, Skin refers to the skin layer enclosing the breast, g to glandular tissue, f to fat tissue, and Gas to the gas in the detector. In addition, t_g and t_f are given by the expressions

$$t_g = \frac{f_g \cdot \rho_f \cdot t_L}{\rho_g + f_g \cdot (\rho_f - \rho_g)}, \tag{6}$$

$$t_f = L - t_g, \tag{7}$$

where ρ_g and ρ_f are the density of glandular and fat tissue[39] and L is the thickness of the breast tissue excluding the skin.

Scatter in the object was not modeled. As described in Sec. II A 1, the detectors are insensitive to photons scattered in the object. The imaging system is photon-counting and does not generate electronic noise. Furthermore, the x-ray detector elements were assumed to be uncorrelated. Scattered photons and fluorescent photons created in the detector were hence assumed to escape the detector altogether and not to generate a secondary signal. This was experimentally verified. In images of a radio-opaque foil positioned on top of the Bucky, the vast majority of the pixels gave a signal intensity of zero, resulting in a scatter to primary ratio less than 1%.

The Sn and Cu DBT images were produced with a shift-and-add algorithm. Signal intensity per pixel in the DBT series $\mathrm{SI}_m(f_g, I)$ is

$$\mathrm{SI}_m(f_g, I) = N \times \exp\left[\frac{1}{N}\sum_{n=1}^{N} P_{m,n}(f_g, I)\right] \tag{8}$$

$$\cong N \times \sum_{i=1\ \mathrm{keV}}^{49\ \mathrm{keV}} S_m(E_i) e^{-\alpha_i}(1 - e^{-\beta_i})\Delta E. \tag{9}$$

The approximation made in Eq. (9) follows from Eq. (3) in conjunction with the assumption that signal intensity in the projection images has negligible angular dependence, so that $P_{m,n}(f_g, I) \cong P_{m,n}(f_g, I)|_{\theta_n = 0}$. This assumption is motivated by the fact that the maximum projection angle is 11°.

It should be pointed out that Eq. (9) is the sum of Poisson distributed random variables over multiple energies. From standard properties, the net sum is also a Poisson process. Recalling Eq. (2) and using Appendix B to calculate the expected value of the logarithm of a Poisson process, mean signal intensity in the DE-DBT image can be determined from the expression

$$\overline{\mathrm{SI}}_{\mathrm{DE}}(f_g, I) \cong \mathrm{In}[\overline{\mathrm{SI}}_{\mathrm{Cu}}(f_g, I)] - w_t \cdot \mathrm{In}[\overline{\mathrm{SI}}_{\mathrm{Sn}}(f_g, I)]. \tag{10}$$

The standard deviation in $\mathrm{SI_{DE}}(f_g, I)$, $\sigma_{\mathrm{DE}}(f_g, I)$, can be calculated as

$$\sigma_{\mathrm{DE}}(f_g, I) \cong \frac{1}{2} \times \left[\frac{1}{2} - \frac{\sqrt{2}}{4}\ln(\sqrt{2} - 1)\right] \times \sqrt{\frac{1}{\overline{\mathrm{SI}}_{\mathrm{Cu}}(f_g, I)} + w_t^2 \frac{1}{\overline{\mathrm{SI}}_{\mathrm{Sn}}(f_g, I)}}. \tag{11}$$

In Eq. (11), the factor of 1/2 accounts for the 2×2 binning of the image data before DBT reconstruction and the second factor accounts for presampling in the reconstruction (Appendix A). In deriving Eq. (11), it has been assumed that the covariance of $\mathrm{SI}_{\mathrm{Cu}}(f_g, I)$ against $\mathrm{SI}_{\mathrm{Sn}}(f_g, I)$ is negligible.

Spectra were computed using an extrapolation of Boone's mammography spectra.[21,37] The raw W-target spectra were

TABLE I. Model parameters used to simulate the DE implementation of the XC Mammo-3T XCounter system.

Specifications of the XC Mammo-3T, XCounter system	
Tube housing	0.79 mm Be window
Source to detector distance	650 mm air
Cu filter	0.11–0.27 mm in 0.01 mm increments
Sn filter	0.08–0.22 mm in 0.01 mm increments
Compression paddle	2 mm PMMA
Detector	Kr gas
Specifications of the x-ray contrast agent	
I	1 mg/cm^2
Specifications of the imaged breasts	
Total breast thickness	20, 40, 60, and 80 mm
Skin	2×4 mm
Glandular tissue fraction f_g [a]	0.00, 0.50, and 1.00

[a]Proportion of glandular tissue mass to total tissue mass in the breast without skin (Ref. 43).

shaped using the Lambert–Beer law with appropriate mass attenuation coefficients and areal densities[40] of the materials and system parameters listed in Table I. The geometry of the breast was modeled as specified by Boone;[41] the breast consists of a mixture of glandular and adipose tissue[39] surrounded by a 4 mm thick skin layer.[40]

II.C. Performance optimization

II.C.1. Weighting factor optimization

Weighting factors w_t were calculated to cancel the contrast between breast tissues with two different mass fractions of glandular tissue f_{g1} and f_{g2}. Optimal w_t values were calculated as[19]

$$w_t = \frac{\ln[\overline{\mathrm{SI}}_{\mathrm{Cu}}(f_{g1},I)] - \ln[\overline{\mathrm{SI}}_{\mathrm{Cu}}(f_{g2},I)]}{\ln[\overline{\mathrm{SI}}_{\mathrm{Sn}}(f_{g1},I)] - \ln[\overline{\mathrm{SI}}_{\mathrm{Sn}}(f_{g2},I)]}. \quad (12)$$

Each (f_{g1},f_{g2}) pair results in a different w_t value. Recognizing that breast tissue is spatially heterogeneous, w_t values were computed for all possible (f_{g1},f_{g2}) combinations. Optimal w_t was computed for all Sn–Cu filter pairs and breast thicknesses listed in Table I.

II.C.2. Image optimization

The SDNR per pixel between iodine-enhanced breast tissue (I) and background breast tissue (B), normalized to the square root of the total mean glandular dose ($\mathrm{MGD_{Total}}$), was computed as the figure of merit for the detectability of iodine in the DE-DBT images. Using Eqs. (10) and (11), the SDNR per pixel was defined as

$$\mathrm{SDNR} = \frac{\overline{\mathrm{SI}}_{\mathrm{DE}}(f_g,0) - \overline{\mathrm{SI}}_{\mathrm{DE}}(f_g,I)}{\sigma_{\mathrm{DE}}(f_g,0)} \quad (13)$$

and $\mathrm{MGD_{Total}}$ was defined as

$$\mathrm{MGD_{Total}} = \mathrm{MGD_{Cu}} + \mathrm{MGD_{Sn}}, \quad (14)$$

where $\mathrm{MGD_{Cu}}$ and $\mathrm{MGD_{Sn}}$ are the MGD allocated to the Sn and the Cu images, respectively. $\mathrm{SDNR}/\sqrt{\mathrm{MGD_{Total}}}$ varies as a function of the dose fraction allocated to the Sn and Cu filtered x-ray beams. Therefore, $\mathrm{SDNR}/\sqrt{\mathrm{MGD_{Total}}}$ was calculated as a function of $\mathrm{MGD_{Cu}}/\mathrm{MGD_{Total}}$

$\mathrm{SDNR}/\sqrt{\mathrm{MGD_{Total}}}$ values were compared for various system configurations. In the first configuration, both the photon fluence and spectrum were controlled by varying the prepatient collimator width for the Sn and Cu filters; hereafter, this is referred to as the *variable* configuration. In this configuration, the fraction of the x-ray beam filtered by Sn and Cu can be varied to maximize $\mathrm{SDNR}/\sqrt{\mathrm{MGD_{Total}}}$, called $\mathrm{SDNR_{max}}/\sqrt{\mathrm{MGD_{Total}}}$. The ratio of the fraction of the x-ray beam assigned to the Sn images to the fraction of the x-ray beam assigned to the Cu images is named the collimator ratio. The variable configuration is hypothetical and not useful in practice because the spatial resolution would be negatively influenced.

Several *fixed* configurations were also investigated. In these configurations, the collimator width and filter thicknesses are held constant; however, the number of collimator slits that are covered with Sn and Cu filters can be varied. In this way, the dose allocation for the low and high-energy images can be varied to a degree. The various fixed configurations studied are hereafter named by the number (N) of fan beams that are alternately filtered with Sn or Cu (i.e., $\mathrm{N_{Sn}}:\mathrm{N_{Cu.}}$).

In the fixed configurations, $\mathrm{SDNR}/\sqrt{\mathrm{MGD_{Total}}}$ was optimized in terms of $\mathrm{MGD_{Total}}$/mA s by varying the Sn and Cu filter thicknesses and the number of fan beams filtered by Sn and Cu. The optimization was conducted within the limitations of the x-ray tube loading. As discussed in Sec. III, the optimum configuration typically required the tube to be op-

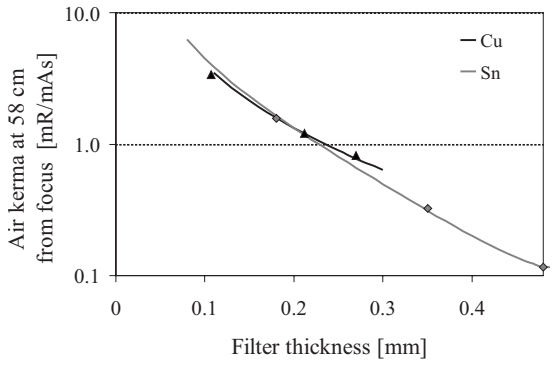

FIG. 3. Air kerma per mAs at 58 cm from the focus of the x-ray source as a function of Sn and Cu filter thickness.

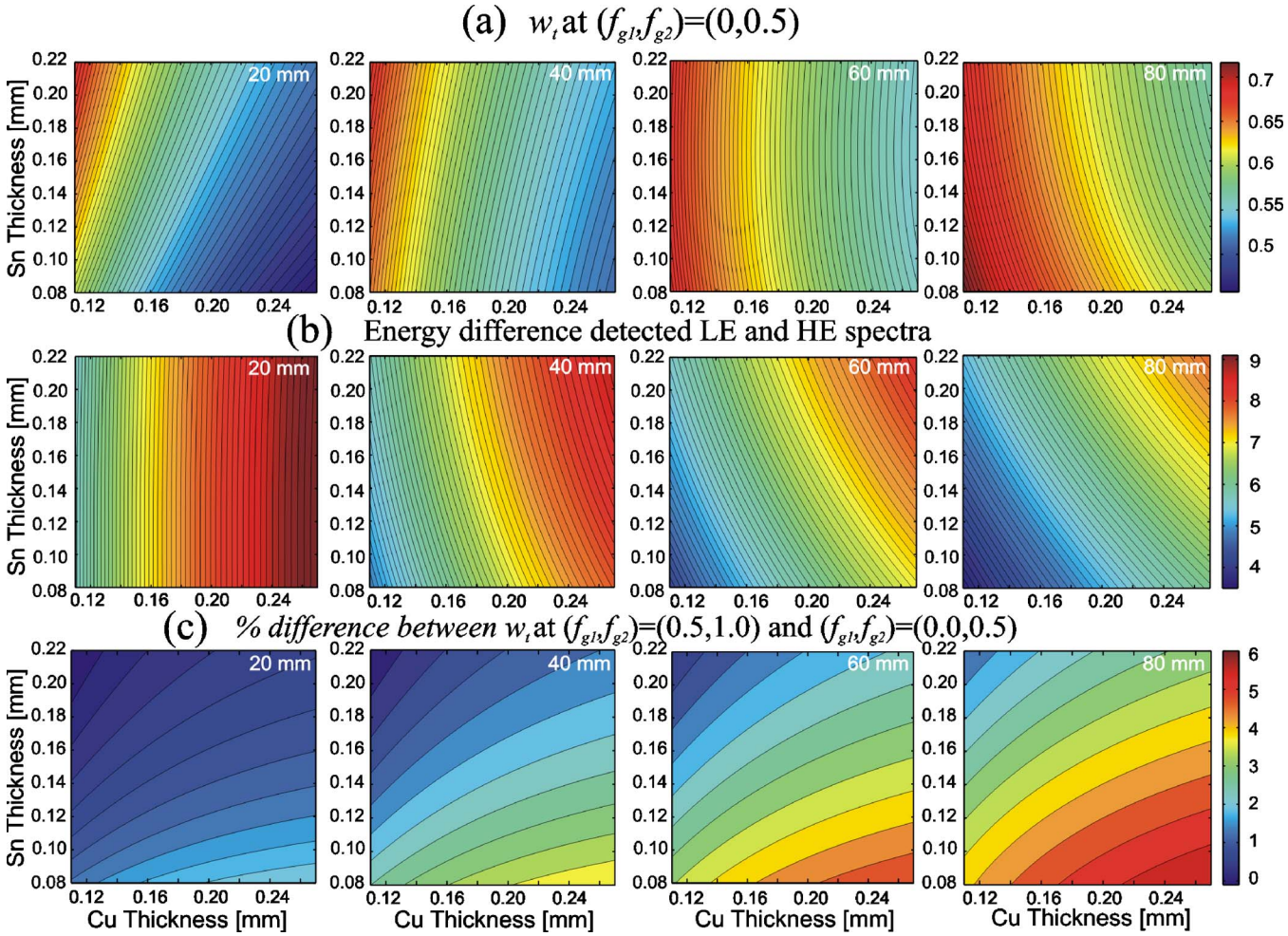

FIG. 4. (a) w_t giving optimal breast tissue cancellation for $(f_{g1},f_{g2})=(0.0,0.5)$. (b) Average energy difference between detected Sn and Cu spectra. (c) Difference (%) between w_t values that optimally cancel $(f_{g1},f_{g2})=(0.0,0.5)$ and $(f_{g1},f_{g2})=(0.5,1.0)$. All results are shown as a function of Sn–Cu filter pair and breast thickness (indicated in white in the upper right corners).

erated at the maximum mA, thus SDNR was calculated for all breast thicknesses at 140 mA.

For all configurations, calculations were performed using the parameters listed in Table I. An iodine concentration of 1 mg/cm^2 was chosen as being typical of that expected clinically.[21] For calculation of SDNR, $f_g=0.5$ was used.

Breast entrance air kerma K of the Sn and Cu spectra were calculated using the method described by Boone[41]

$$K(S,L+t_{\mathrm{Skin}},f_g)=\frac{\mathrm{MGD}_j}{pDgN(S_m,L+t_{\mathrm{Skin}},f_g)}, \quad (15)$$

where MGD_m denotes the MGD allocated to the Sn or Cu images, $pDgN$ is the MGD per unit breast entrance dose, S_m refers to the Sn or Cu breast entrance spectra, and $L+t_{\mathrm{Skin}}$ indicates the total breast thickness.

To obtain $\mathrm{MGD}_{\mathrm{Sn}}$/mAs and $\mathrm{MGD}_{\mathrm{Cu}}$/mAs, experimentally measured tube outputs (K/mAs) for the studied Sn and Cu filters were multiplied with appropriate $pDgN(S_m,L+t_{\mathrm{Skin}},f_g)$ factors. Tube output (K/mAs) was measured by scanning the 48 fan beams over an air ionization chamber and electrometer (Radcal 10X5–6M and MDH1515; Radcal Corporation, Monrovia, CA) operated in integration mode. Tube output was measured with filtration of 0.185, 0.356, and 0.485 mm Sn and 0.107, 0.185, 0.212, and 0.27 mm Cu. A least-squares power fit was applied to obtain tube outputs for all studied Sn and Cu filters (Fig. 3). The inverse square law was applied to calculate the entrance exposure for various breast thicknesses.

III. RESULTS AND DISCUSSION

III.A. Weighting factor optimization

Figures 4 and 5 summarize w_t for the studied Sn–Cu filter pairs, breast thicknesses, and breast tissue compositions (f_{g1},f_{g2}). Figure 4(a) shows w_t values that optimally suppress breast tissue compositions $(f_{g1},f_{g2})=(0,0.5)$ for all Sn–Cu filtration pairs and the four breast thicknesses under study. For a given filter pair, w_t values are smaller for thinner breasts. For all breast thicknesses, optimal w_t varies greatly as a function of Cu thickness. Observe that for 60 mm thick breasts, the magnitude of w_t is almost independent of Sn thickness, while for 20, 40, and 80 mm breasts, w_t varies somewhat with Sn thickness. To understand these data, the average energy differences between the detected Sn and Cu

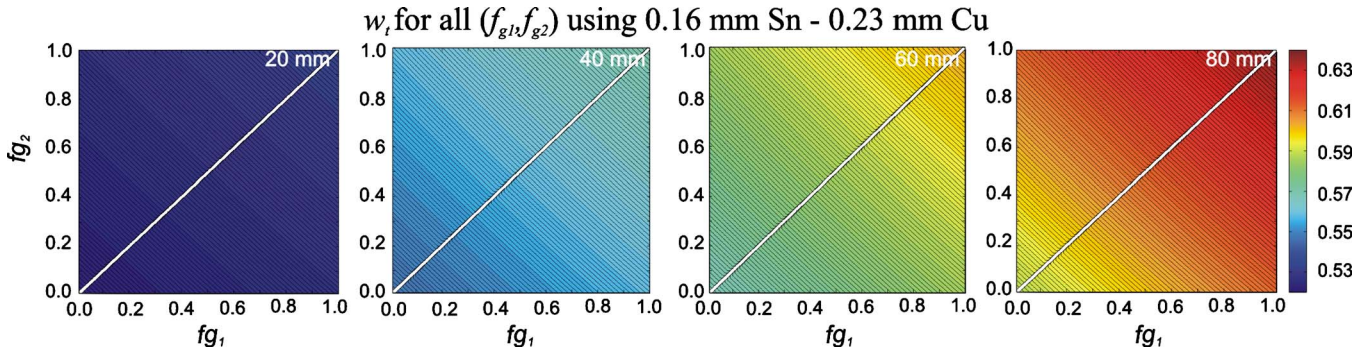

FIG. 5. w_t giving optimal breast tissue cancellation as a function of (f_{g1},f_{g2}) using a 0.16 mm Sn–0.23 mm Cu filter pair. Results are shown for breast thicknesses of 20, 40, 60, and 80 mm.

spectra were calculated [Fig. 4(b)]. Comparison of Figs. 4(a) and 4(b) shows that w_t is related to the average energy difference between the detected Sn and Cu x-ray beams. In particular, the Sn image has to be multiplied with a higher w_t to cancel the breast background anatomy when the energy difference between the Sn and Cu x-ray beams becomes smaller. To provide further insight into this phenomenon, the average energies of the detected Sn and Cu x-ray spectra were determined. By increasing the Cu thickness from 0.11 to 0.27 mm, the average energy of the detected Cu spectrum increases by 3.4, 3.0, 2.7, and 2.4 keV for 20, 40, 60, and 80 mm thick breasts. By increasing the Sn thickness from 0.08 to 0.22 mm, the average energy of the detected Sn spectrum decreases by 0.1, 0.2, 1.4, and 1.7 keV for 20, 40, 60, and 80 mm thick breasts. The average energy increase of the detected Cu spectra with Cu thickness is anticipated; however, the decrease in the average energy of the detected Sn spectra with increasing Sn thickness requires a close examination of the Sn spectra. A non-negligible fraction of the Sn spectrum occurs above the K-edge of Sn. For a given breast thickness, increasing the thickness of the Sn filter suppresses the part of the spectrum above the K-edge of Sn and in turn decreases the average energy of the spectrum. When the Sn filter thickness is increased from 0.08 to 0.22 mm, the fraction of the spectrum below the K-edge of Sn increases from 72% to 88% for 20 mm thick breasts and from 51% to 75% for 80 mm breasts.

Figure 5 shows w_t values that optimally suppress all possible breast tissue compositions (f_{g1},f_{g2}) for the 0.16 mm Sn–0.23 mm Cu filter combination. We show later on that this filter combination is optimal. We believe it is the most appropriate example to illustrate our work. Optimal w_t increases when either f_{g1} or f_{g2} increase. Figure 5 also shows that the value of w_t, which cancels any possible breast tissue glandularity, varies by less than 1% for 20 mm thick breasts and less than 18% for 80 mm. These results are consistent with those in Fig. 4(c), which show that the w_t to cancel $(f_{g1},f_{g2})=(0.5,1.0)$ is larger than the w_t to cancel $(f_{g1},f_{g2})=(0,0.5)$ for all Sn–Cu filter combinations. The difference increases with increasing Cu and decreasing Sn thicknesses. As a result, weighted logarithmic subtraction will be superior for thin breasts because w_t is almost independent of breast tissue composition. For thicker breasts, weighted logarithmic subtraction will result in some background structure, unless w_t is adjusted locally for composition. In addition, to optimally cancel background breast structure, smaller w_t values should be applied at the margin of the breasts where the breast is thinner than in the center.

III.B. Image optimization

Figure 6 illustrates $\mathrm{SDNR}/\sqrt{\mathrm{MGD}_{\mathrm{Total}}}$ as a function of $\mathrm{MGD}_{\mathrm{Cu}}/\mathrm{MGD}_{\mathrm{Total}}$ and Cu thickness for a 40 mm thick breast with a 0.16 mm Sn filter. $\mathrm{SDNR}_{\mathrm{max}}/\sqrt{\mathrm{MGD}_{\mathrm{Total}}}$ obtained with the variable configuration are shown as a solid line. The 3:1, 2:1, 1:1, 1:2, and 1:3 fixed configurations are shown as broken lines. $\mathrm{SDNR}/\sqrt{\mathrm{MGD}_{\mathrm{Total}}}$ has a broad peak as a function of $\mathrm{MGD}_{\mathrm{Cu}}/\mathrm{MGD}_{\mathrm{Total}}$, although the values decline rapidly for extreme values of $\mathrm{MGD}_{\mathrm{Cu}}/\mathrm{MGD}_{\mathrm{Total}}$. The 1:2 fixed configuration gives $\mathrm{SDNR}/\sqrt{\mathrm{MGD}_{\mathrm{Total}}}$ values within 15% of $\mathrm{SDNR}_{\mathrm{max}}/\sqrt{\mathrm{MGD}_{\mathrm{Total}}}$, and thus was judged to be superior to the other configurations for these filter combinations.

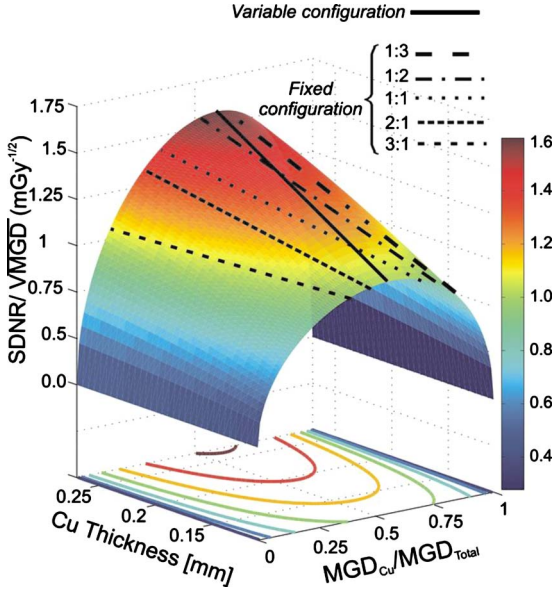

FIG. 6. $\mathrm{SDNR}/\sqrt{\mathrm{MGD}_{\mathrm{Total}}}$ between 1 mg/cm^2 iodine-enhanced and nonenhanced 40 mm thick breast tissue as a function of $\mathrm{MGD}_{\mathrm{Cu}}/\mathrm{MGD}_{\mathrm{Total}}$ and Cu filter thickness. A 0.16 mm Sn filter was used. The lines drawn on the surface indicate $\mathrm{SDNR}/\sqrt{\mathrm{MGD}_{\mathrm{Total}}}$ for various fixed system configurations.

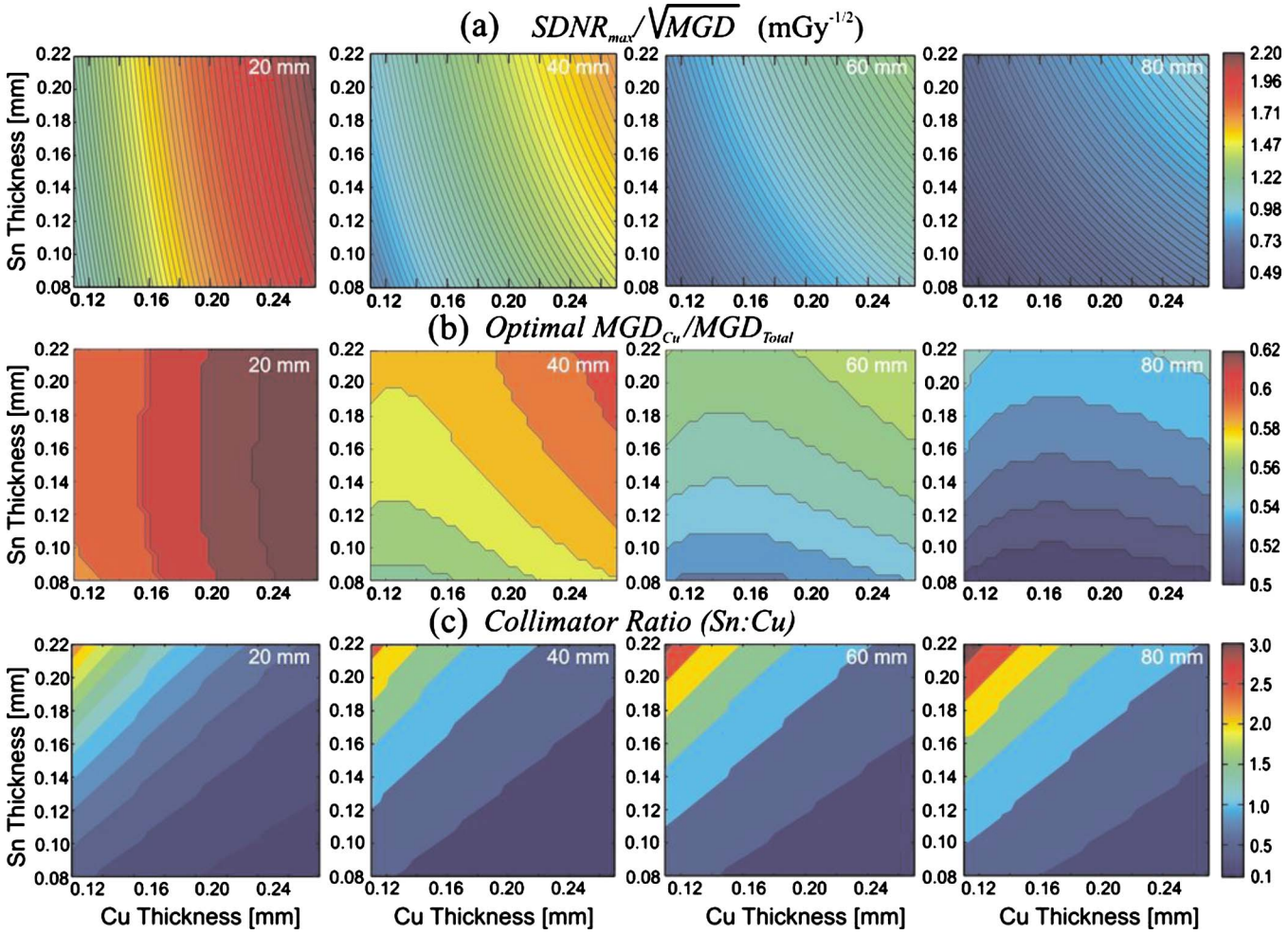

FIG. 7. (a) $SDNR_{max}/\sqrt{MGD_{Total}}$ between 1 mg/cm^2 iodine-enhanced and nonenhanced breast tissue, (b) optimal MGD_{Cu}/MGD_{Total}, and (c) collimator ratios for the variable configuration as a function of Sn–Cu filter pair and breast thickness (indicated in the upper right corner). The calculations were performed for breasts with glandular tissue fraction f_g=0.5.

Figures 7(a) and 7(b) show the dependence of $SDNR_{max}/\sqrt{MGD_{Total}}$ and optimal MGD_{Cu}/MGD_{Total} on Sn–Cu filtration for the variable configuration for 20, 40, 60, and 80 mm thick breasts. For 20 mm thick breasts, $SDNR_{max}/\sqrt{MGD_{Total}}$ is almost independent of Sn thickness. With increasing breast thickness, the dependence of $SDNR_{max}/\sqrt{MGD_{Total}}$ on Sn filter thickness increases. Optimal MGD_{Cu}/MGD_{Total} values are smaller for thicker breasts. For 20 mm thick breasts, the optimal MGD_{Cu}/MGD_{Total} is almost independent of Sn thickness. For 40 and 60 mm thick breasts, the optimal MGD_{Cu}/MGD_{Total} varies as a function of Sn and Cu thickness. For 80 mm thick breasts, the optimal MGD_{Cu}/MGD_{Total} is almost independent of Cu thickness. As shown in Fig. 7(b), the optimal MGD_{Cu}/MGD_{Total} values are greater than 0.5 for all conditions.

Figure 7(c) shows the collimator ratios for the variable configuration for 20, 40, 60, and 80 mm thick breasts. These data support the use of the 1:2 (Sn:Cu) fixed configuration. As a result of these data, the 1:2 (Sn:Cu) configuration was selected as being the most practical system configuration. Figures 8(a) and 8(b) show the dependence of $SDNR/\sqrt{MGD_{Total}}$ and corresponding MGD_{Cu}/MGD_{Total} as a function of Sn–Cu filtration for the 1:2 fixed configuration. For most Sn–Cu filter pairs, $SDNR/\sqrt{MGD_{Total}}$ exceeds 85% of $SDNR_{max}/\sqrt{MGD_{Total}}$ (regions between the dotted lines for 20 and 40 mm thick breasts and regions below the dotted lines for 60 and 80 mm thick breast). This is attributable to the fairly broad maximum of $SDNR/\sqrt{MGD_{Total}}$ for intermediate dose allocations as illustrated in Fig. 6.

Figure 8(c) shows the dependence of MGD_{Total}/mA s on Sn–Cu filtration for the 1:2 configuration. MGD_{Total}/mA s decreases with increasing Sn and Cu filter thicknesses. The low MGD_{Total}/mA s values can be attributed to the fact that approximately 90% of the generated x rays are absorbed by the prepatient collimator.

SDNR values were calculated at the maximum feasible tube loading, i.e., 140 mA [Fig. 8(d)]. Even at 140 mA, MGD_{total} values are lower than the typical MGD applied to acquire a single mammogram.[42] For all filter combinations, MGD_{total} is less than 2.03, 1.84, 1.64, and 1.48 mGy for 20, 40, 60, and 80 mm thick breasts. SDNR varies slowly as a function of Sn–Cu filtration; the variation in SDNR is smaller for thicker breasts. The variation in SDNR as a function of Sn–Cu filtration is governed by a trade-off between

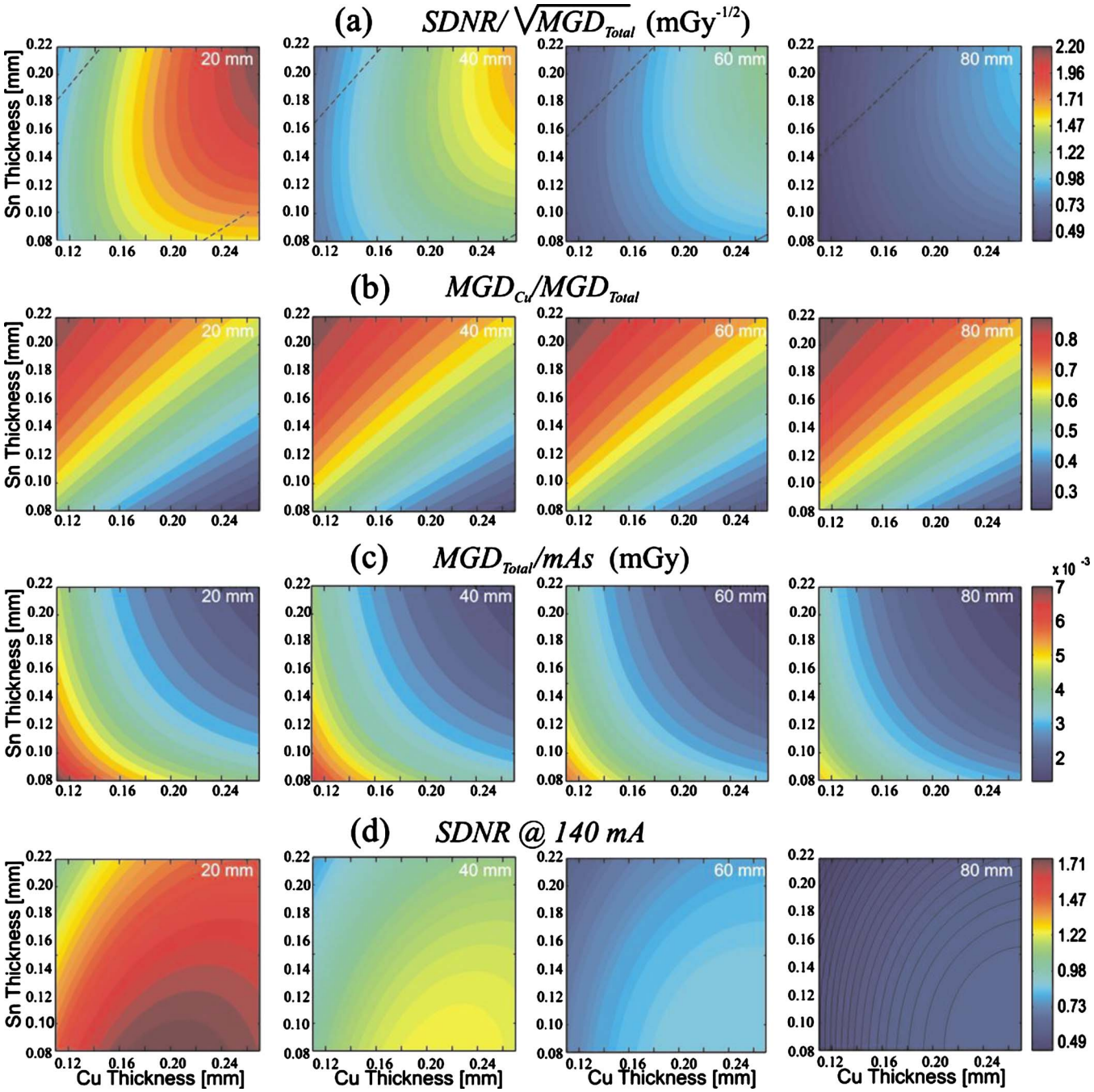

FIG. 8. (a) SDNR/$\sqrt{\text{MGD}_{\text{Total}}}$ between 1 mg/cm^2 iodine-enhanced and nonenhanced breast tissue, (b) $\text{MGD}_{\text{Cu}}/\text{MGD}_{\text{Total}}$, (c) $\text{MGD}_{\text{Total}}$/mA s, and (d) SDNR at 140 mA as a function of Sn–Cu filter pair and breast thickness for the 1:2 fixed system configuration. The calculations were performed for breasts with glandular tissue fraction f_g=0.5. In (a), the region where SDNR/$\sqrt{\text{MGD}_{\text{Total}}}$ exceeds 85% of $\text{SDNR}_{\text{max}}/\sqrt{\text{MGD}_{\text{Total}}}$ occurs between the dotted lines for 20 and 40 mm thick breasts and below the dotted lines for 60 and 80 mm thick breast.

iodine contrast and noise; increasing the Sn and Cu filter thickness gives better spectral separation, resulting in a greater iodine contrast, but also results in greater image noise. SDNR peaks at a different Sn–Cu filter combination for each breast thickness; as breast thickness increases, the peak Cu filtration increases.

Based on maximizing SDNR/$\sqrt{\text{MGD}_{\text{Total}}}$ at 140 mA, constrained to integer steps in flux allocation between the Cu an Sn images, a filter pair of 0.16 mm Sn and 0.23 mm Cu was selected as providing the best possible performance for breasts of different thicknesses and compositions. This filter pair gives SDNR values that are only 3% (20 mm breast) to 8% (80 mm breast) lower than the peak SDNR. Table II summarizes for the selected Sn–Cu filter combination w_t, SDNR, $\text{MGD}_{\text{Cu}}/\text{MGD}_{\text{Total}}$, and $\text{MGD}_{\text{total}}$ for 20–80 mm thick breasts. Note that the reasonably low $\text{MGD}_{\text{total}}$ will permit multiple images to be acquired, from which temporal information can be derived.

TABLE II. Optimal w_t, SDNR and MGD_{Total} at 140 mA for the most practical system configuration, i.e., the 1:2 (Sn:Cu) system configuration using 0.16 mm Sn and 0.23 mm Cu filters. The calculations were performed for breasts with glandular tissue fraction f_g=0.5. The criterion to obtain the feasible operating points is given in the text.

Breast thickness (mm)	w_t	SDNR at 1 mg I/cm^2	MGD_{Total} (mGy)
20	0.52	1.64	0.70
40	0.55	1.20	0.65
60	0.58	0.87	0.59
80	0.60	0.61	0.53

IV. CONCLUSIONS

In this work, theoretical modeling was performed to develop a DE acquisition technique for iodine-enhanced imaging using a photon-counting DBT system. System configuration and technique parameters were investigated to provide optimal SDNR in iodine-enhanced DE-DBT images at an acceptable MGD using practice tube loadings.

It was found that weighted logarithmic subtraction is superior for thin breasts because w_t is almost independent of breast tissue composition. For thicker breasts, w_t varies more with breast tissue composition resulting in poorer suppression of background structure, unless w_t is adjusted locally for composition. Our results also suggest that to cancel the background breast structure optimally, smaller w_t values should be applied at the margin of the breasts.

It was found that a configuration whereby one collimator slit is covered with a Sn filter alternated with two collimator slits covered with a Cu filter gives near optimal SDNR. A 0.16 mm Sn and 0.23 mm Cu filter combination was found to provide the best possible performance for breasts of different thicknesses and compositions. Our results encourage further investigation and optimization of DE CE-DBT as a diagnostic tool for breast cancer detection and differentiation.

ACKNOWLEDGMENTS

The authors acknowledge the financial support of XCounter, Philips Medical Systems/RSNA Research Seed Grant 2005, the Department of Defense Concept Award No. W81XWH-06-1-0613, and the National Cancer Institute Grant No. PO1-CA85484.

APPENDIX A: COMPUTATION OF FACTOR IN STANDARD DEVIATION OF $SI_{DE}(f_g, l)$ ACCOUNTING FOR PRESAMPLING IN THE RECONSTRUCTION

Resampling in the shift-and-add algorithm is illustrated in Fig. 9(a). Consider two projection images of an unknown object, projection n and Projection n', acquired at different angles. Projection n and Projection n' depict the object at different positions, as illustrated by the colored pixels in Fig. 9(a). To reconstruct the image plane with this unknown object in focus, Projection n' should be shifted with respect to Projection n to have the shadows registered. Before Projections n and n' can be added, however, Projection n' should be resampled so as to have the pixels of Projection n and Projection n' registered. The signal intensity in the resampled Projection P_{RS_i} using a sampling factor x can be written as

$$P_{RS_i} = x \cdot P_i + (1-x) \cdot P_{i+1}, \quad 0 \le x \le 1, \tag{A1}$$

where i and $i+1$ refer to neighboring pixels. The notation n' is dropped here for clarity. Assuming P_i and P_{i+1} are the logarithm of Poisson distributed random variables, the standard deviation in P_{RS_i} is given by

$$\sigma_{P,RS} = \sqrt{\frac{x^2}{\bar{P}_i} + \frac{(1-x)^2}{\bar{P}_{i+1}}}. \tag{A2}$$

Equation (A2) incorporates the fact that the covariance of P_i against P_{i+1} is negligible. The dependence on σ_{RS} is shown in Fig. 9(b). Presuming that x is uniformly distributed be-

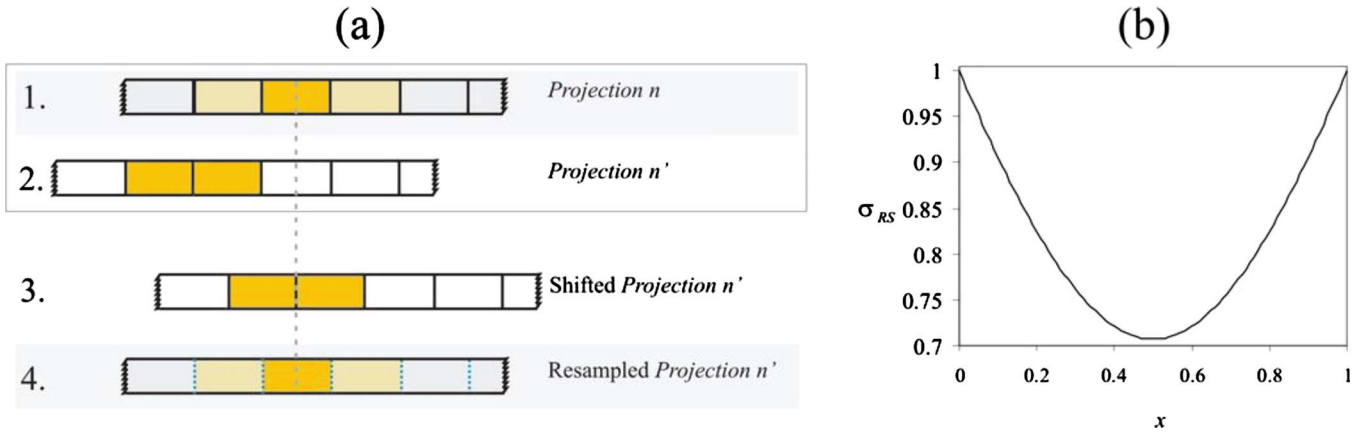

FIG. 9. (a) Principle of resampling when using the shift-and-add algorithm. Projection n (1) and projection n' (2) are projection images acquired at two different angles. The colored pixels represent the shadow of an unknown object. To reconstruct the image with the object in focus, Projection n' is shifted with respect to Projection n to have the shadows registered (3). Projection n' is then resampled to have the pixels of Projection n and Projection n' registered (4). (b) Standard deviation in the SI of the resampled projection image as a function of x, the resampling factor.

tween 0 and 1, the average standard deviation of P_{RS_i} in the resampled image is thus

$$\bar{\sigma}_{P,RS} = \int_0^1 \sqrt{\frac{x^2}{\bar{P}_i} + \frac{(1-x)^2}{\bar{P}_{i+1}}}\,dx. \tag{A3}$$

In acquiring projection images of a homogenous object, $\bar{P}_i = \bar{P}_{i+1} = \bar{P}$, resulting in

$$\bar{\sigma}_{P,RS} = \sqrt{\frac{1}{\bar{P}}} \cdot \left[\frac{1}{2} - \frac{\sqrt{2}}{4}\ln(\sqrt{2}-1)\right]. \tag{A4}$$

APPENDIX B: EXPECTED VALUE OF THE LOGARITHM OF A POISSON PROCESS

In the body of this work, Eq. (10) is derived assuming that $\langle \ln[\mathrm{SI}_m(f_g,I)]\rangle$ is well approximated by $\ln[\overline{\mathrm{SI}}_m(f_g,I)]$. We now provide an analytical justification for this property.

Suppose that a discrete random variable k is Poisson-distributed with mean λ, as is the case for $\mathrm{SI}_m(f_g,I)$. Denoting P_k as the probability mass function, it follows that

$$\langle \ln k\rangle = \sum_k P_k \ln k. \tag{B1}$$

Although the summation in Eq. (B1) is performed in theory over infinitely many k, it may be performed in practice over all k within j standard deviations (σ) of λ, where j is chosen to be sufficiently large (e.g., $j=5$) so that excluding terms has a negligible effect. Equation (B1) can now be approximated using the Taylor expansion of $\ln k$ about $k=\lambda$

$$\ln k = \ln\lambda + \sum_{n=1}^{\infty} \frac{(-1)^{n+1}(k-\lambda)^n}{n\lambda^n}, \tag{B2}$$

where convergence occurs in the interval $k \in (0, 2\lambda]$. With $j=5$ and $\overline{\mathrm{SI}}_m(f_g,I)$ no less than approximately 500 in this study, it can be shown that all k within $j\sigma$ of λ fall in this interval. Inserting Eq. (B2) to first order into Eq. (B1) yields

$$\langle \ln k\rangle \approx (-1+\ln\lambda)\sum_k P_k + \frac{1}{\lambda}\sum_k P_k k \tag{B3}$$

$$\approx (-1+\ln\lambda)(1) + \frac{1}{\lambda}(\lambda) \tag{B4}$$

$$= \ln\lambda. \tag{B5}$$

It is now worthwhile to quantify the error conferred by this approximation. According to Taylor's theorem, there exists a z between k and λ such that the Lagrange form of the remainder associated with the first order approximation of $\ln k$ is

$$R_2(k) = \frac{-(k-\lambda)^2}{2z^2}. \tag{B6}$$

Assuming that k is within $j\sigma$ of λ, the remainder is maximized with $z=\lambda - j\sqrt{\lambda}$. From this observation and the property that P_k is positive, it follows that the absolute error $|E|$ in approximating $\langle \ln k\rangle$ with $\ln\lambda$ satisfies the inequality

$$|E| \le \frac{1}{2(\lambda - j\sqrt{\lambda})^2}\sum_k P_k(k-\lambda)^2 \tag{B7}$$

$$\le \frac{\lambda}{2(\lambda - j\sqrt{\lambda})^2} \tag{B8}$$

$$\sim \frac{1}{2\lambda}, \quad \lambda \text{ large}, \tag{B9}$$

where we have incorporated the fact that the variance (σ^2) of P_k, which is recovered by the summation in Eq. (B7), is equivalent to λ. To illustrate the calculation of this error, suppose that λ is 500 and that j is 5. It can be shown that $\langle \ln k\rangle$ and $\ln\lambda$ are 6.213 60 and 6.214 61, respectively, making $|E|=0.001\,01$ and the relative error 0.016%. Equation (B8) correctly calculates 0.001 66 as an upper bound for $|E|$ and Eq. (B9) accurately approximates $|E|$ as 0.001.

With increasing λ, Eq. (B8) predicts an even smaller upper limit for $|E|$. Hence, for the purpose of this work, $\langle \ln k\rangle$ can be approximated by $\ln\lambda$ with negligible error.

[a]Author to whom correspondence should be addressed. Electronic mail: Andrew.Maidment@uphs.upenn.edu; Telephone: +1-215-746-8763; Fax: +1-215-746-8764.

[1]N. Weidner, J. P. Semple, W. R. Welch, and J. Folkman, "Tumor angiogenesis and metastasis: Correlation in invasive breast carcinoma," N. Engl. J. Med. **324**, 1–8 (1991).
[2]N. M. Hylton, "Vascularity assessment of breast lesions with gadolinium-enhanced MR imaging," Magn. Reson Imaging Clin. N. Am. **9**, 321–331 (2001).
[3]C. K. Kuhl, H. H. Schild, and N. Morakkabati, "Dynamic bilateral contrast-enhanced MR imaging of the breast: Trade-off between spatial and temporal resolution," Radiology **263**, 789–800 (2005).
[4]M. D. Schnall *et al.*, "Diagnostic architectural and dynamic features at breast MR imaging: Multicenter study," Radiology **238**, 42–53 (2006).
[5]D. Saslow *et al.* "American Cancer Society guidelines for breast screening with MRI as an adjunct to mammography," Ca-Cancer J. Clin. **57**, 75–89 (2007).
[6]T. C. Williams, W. B. DeMartini, S. C. Partridge, S. Peacock, and C. D. Lehman, "MR breast imaging computer-aided evaluation program for discriminating benign from malignant lesions," Radiology **244**, 94–103 (2007).
[7]J. Chang *et al.*, "Computed tomographic mammography using a conventional body scanner," AJR, Am. J. Roentgenol. **138**, 553–558 (1982).
[8]S. L. Fritz, C. H. J. Chang, and W. H. Livingston, "Scatter/primary ratio for x-ray spectra modified to enhance iodine contrast in screen-film mammography," Med. Phys. **10**, 866–870 (1983).
[9]A. C. Watt *et al.*, "Breast lesions: Differential diagnosis using digital subtraction angiography," Radiology **159**, 39–42 (1986).
[10]F. Diekmann and U. Bick, "Tomosynthesis and contrast-enhanced digital mammography: Recent advances in digital mammography," Eur. Radiol. **17**, 3086–3092 (2007).
[11]M. Skarpathiotakis *et al.*, "Development of contrast digital mammography," Med. Phys. **29**, 2419–2426 (2002).
[12]R. A. Jong *et al.*, "Contrast-enhanced digital mammography: Initial clinical experience," Radiology **228**, 842–850 (2003).
[13]J. M. Lewin, P. K. Isaacs, V. Vance, and F. J. Larke, "Dual-energy contrast-enhanced digital subtraction mammography: Feasibility," Radiology **229**, 261–268 (2003).
[14]F. Diekmann *et al.*, "Use of iodine-based contrast media in digital full-field mammography—Initial experience," Rofo Fortschr Geb Rontgenstr Neuen Bildgeb Verfahr **175**, 342–345 (2003).
[15]G. Ullman, M. Sandborg, D. Dance, M. Yaffe, and G. Alm Carlsson, "A search for optimal x-ray spectra in iodine contrast media mammography," Phys. Med. Biol. **50**, 3143–3152 (2005).

[16]H. Bornefalk, M. Hemmendorff, and T. Hjärn, "Dual-energy imaging using a digital scanned multi-slit system for mammography: Evaluation of a differential beam filtering technique," in *Proceedings of the Medical Imaging 2006 Conference: Physics of Medical Imaging*, Vol. 6142, edited by M. J. Flynn and J. Hsieh (SPIE, San Diego, 2006).
[17]P. Baldelli *et al.*, "Evaluation of the minimum iodine concentration for contrast-enhanced subtraction mammography," Phys. Med. Biol. **51**, 4233–4251 (2006).
[18]S. Puong, X. Bouchevreau, F. Patoureaux, R. Iordache, and S. Muller, in *Proceedings of the Medical Imaging 2007 Conference: Physics of Medical Imaging*, edited by J. Hsieh and M. J. Flynn (SPIE, San Diego, 2007).
[19]H. Bornefalk, M. Hemmendorff, and T. Hjärn, "Contrast-enhanced dual-energy mammography using a scanned multislit system: Evaluation of a differential beam filtering technique," J. Electron. Imaging **16**, 023001 (2007).
[20]I. Rosado-Méndez, B. A. Palma, and M. E. Brandana, "Analytical optimization of digital subtraction mammography with contrast medium using a commercial unit," Med. Phys. **35**, 5544–5557 (2008).
[21]A.-K. Carton, J. Li, M. Albert, S. Chen, and A. D. Maidment, in *Proceedings of the Medical Imaging 2006 Conference: Physics of Medical Imaging*, edited by M. J. Flynn and J. Hsieh (SPIE, San Diego, 2006), pp. 111–121.
[22]A.-K. Carton, J. Li, S. C. Chen, E. F. Conant, and A. D. A. Maidment, "Optimization of contrast-enhanced digital breast tomosynthesis," Lect. Notes Comput. Sci. **4046**, 183–189 (2006).
[23]S. C. Chen, A.-K. Carton, M. Albert, E. F. Conant, M. D. Schnall, and A. D. A. Maidment, "Initial clinical experience with contrast-enhanced digital breast tomosynthesis," Acad. Radiol. **14**, 229–238 (2007).
[24]A. K. Carton, K. Lindman, C. K. Ullberg, and T. Francke, "Dual-energy subtraction for contrast enhanced digital breast tomosynthesis," in *Proceedings of the Medical Imaging 2007 Conference: Physics of Medical Imaging*, edited by J. Hsieh and M. J. Flynn (SPIE, San Diego, 2007).
[25]S. Puong, F. Patoureaux, R. Iordache, and S. Muller, "Dual-energy contrast enhanced digital breast tomosynthesis: Concept, method, and evaluation on phantoms," in *Proceedings of the Medical Imaging 2007 Conference: Physics of Medical Imaging*, edited by J. Hsieh and M. J. Flynn (SPIE, San Diego, 2007).
[26]A.-K. Carton, C. Ullberg, K. Lindman, T. Francke, and A. D. A. Maidment, "Optimization of a dual-energy contrast-enhanced technique for a photon counting digital breast tomosynthesis system," Lect. Notes Comput. Sci. **5116**, 116–123 (2008).
[27]A.-K. Carton, J. A. Currivan, E. F. Conant, and A. D. A. Maidment, "Temporal subtraction versus dual-energy contrast-enhanced digital breast tomosynthesis: A pilot study," Lect. Notes Comput. Sci. **5116**, 166–173 (2008).
[28]A. K. Carton, S. C. Gavenonis, J. A. Currivan, E. F. Conant, M. D. Schnall, and A. D. A. Maidment, "Dual-energy contrast-enhanced digital breast tomosynthesis—A feasibility study," Br. J. Radiol. **83**, 344–350 ().
[29]A. L. C. Kwan, J. M. Boone, H. Le-Petross, K. K. Lindfors, J. A. Seibert, and J. M. Lewin, "Contrast-enhanced dual-energy digital subtraction mammography: Optimization of the beam energy," in *Proceedings of the Medical Imaging 2005 Conference: Physics of Medical Imaging*, edited by M. J. Flynn (SPIE, San Diego, 2005), pp. 1317–1321.
[30]K. K. Lindfors, J. M. Boone, T. N. Nelson, K. Yang, A. L. C. Kwan, and D. F. Miller, "Dedicated breast CT: Initial clinical experience," Radiology **246**, 725–733 (2008).
[31]D. Lam, A. K. Carton, and A. D. A. Maidment, "Motion correction in temporal subtraction contrast-enhanced digital breast tomosynthesis," in *Tomosynthesis Imaging Symposium 2009: Frontiers in Research and Clinical Applications*, Duke University, Durham, NC, 2009.
[32]S. Thunberg *et al.*, "Evaluation of a photon counting mammography system," in *Proceedings of the Medical Imaging 2002 Conference: Physics of Medical Imaging*, 4682, edited by L. E. Antonuk and M. J. Yaffe (SPIE, San Diego, 2002).
[33]S. J. Thunberg *et al.*, "Dose reduction in mammography with photon counting imaging," in *SPIE Medical Imaging 2004* (SPIE, San Diego, 2004), pp. 457–465.
[34]A. D. A. Maidment *et al.*, "Evaluation of a photon-counting breast tomosynthesis imaging system," in *Proceedings of the Medical Imaging 2005 Conference: Physics of Medical Imaging*, Vol. 5745, edited by M. J. Flynn (SPIE, San Diego, 2005), pp. 572–582.
[35]A. D. A. Maidment *et al.*, "Clinical evaluation of a photon-counting tomosynthesis mammography system," Lect. Notes Comput. Sci. **40461**, 144–151 (2006).
[36]A. D. A. Maidment *et al.*, "Evaluation of a photon-counting breast tomosynthesis imaging system," in *Proceedings of the Medical Imaging 2006 Conference: Physics of Medical Imaging*, edited by M. J. Flynn and J. Hsieh (SPIE, San Diego, 2006).
[37]J. M. Boone, T. R. Fewell, and R. J. Jennings, "Molybdenum, rhodium, and tungsten anode spectral models using interpolating polynomials with application to mammography," Med. Phys. **24**, 1863–1874 (1997).
[38]T. Wu, R. H. Moore, E. A. Rafferty, and D. A. Kopans, "A comparison of reconstruction algorithms for breast tomosynthesis," Med. Phys. **31**, 2636–2647 (2004).
[39]G. R. Hammerstein, D. W. Miller, and D. R. White, "Absorbed radiation dose in mammography," Radiology **130**, 485–491 (1979).
[40]http://physics.nist.gov/PhysRefData/XrayMassCoef/cover.html
[41]J. M. Boone, "Normalized glandular dose (DgN) coefficients for arbitrary x-ray spectra in mammography: Computer-fit values of Monte Carlo derived data," Med. Phys. **29**, 869–875 (2002).
[42]Mammography ACoQAi, *Mammography Quality Control Manual* (American College of Radiology, Reston, 1999).
[43]J. M. Boone, "Glandular breast dose for monoenergetic and high-energy x-ray beams: Monte Carlo assessment," Radiology **213**, 23–37 (1999).